Platinum-loaded lanthanum-doped calcium titanate photocatalysts prepared by a flux method for photocatalytic steam reforming of methane

Akihiko Anzai,[a] Kenji Fujiwara,[a] Akira Yamamoto,[a,b] and Hisao Yoshida[a,b]*

Affiliation and full postal address

[a] *Department of Interdisciplinary Environment, Graduate School of Human and Environmental Studies, Kyoto University, Yoshida Nihonmatsu-cho, Sakyo-ku, Kyoto 606-8501, Japan*

[b] *Elements Strategy Initiative for Catalysts & Batteries (ESICB), Kyoto University, Kyotodaigaku Katsura, Nishikyo-ku, Kyoto 615-8520, Japan*

Corresponding author

Professor Hisao Yoshida

Department of Interdisciplinary Environment, Graduate School of Human and Environmental Studies, Kyoto University, Yoshida Nihonmatsu-cho, Sakyo-ku, Kyoto 606-8501, Japan

Tel: +81–75–753–6594 Fax: +81–75–753–2988

E–mail address: yoshida.hisao.2a@kyoto-u.ac.jp

Abstract

Calcium titanate ($CaTiO_3$) samples were prepared by a flux method with various parameters such as the selection of the flux, presence or absence of the flux, and solute concentration in the molten mixture with the flux. These conditions much influenced the structural and physical properties like morphology, particle size, specific surface area, and photoabsorption bands. The photocatalytic activity of the samples loaded with Pt-cocatalyst ($Pt/CaTiO_3$) were evaluated for the photocatalytic steam reforming of methane around room temperature. It was found that the sample prepared by the flux method realized 3.3 times higher photocatalytic activity than that by a conventional solid state reaction method. Further, La-doping to the $CaTiO_3$ photocatalyst ($Pt/CaTiO_3$:La) was examined. It was revealed that La cation was successfully doped at the Ca site in the $CaTiO_3$ lattice. It is observed that small amount of La-doping anomalously enhanced the crystal growth although it lowered the photocatalytic activity. In contrast, the sample with a moderate amount of La-doping such as 1 mol% exhibited 1.6 times higher photocatalytic activity than the non-doped sample. Although most of the structural properties such as morphology, particle size and the specific surface area could not simply explain the improvement of photocatalytic activity, at least it was revealed that the defects giving rise to the absorption bands in visible light region decreased the photocatalytic activity.

Keywords: methane conversion; hydrogen production; calcium titanate; flux method; lanthanum doping; crystal growth

1. Introduction

Hydrogen has been used as an important chemical intermediate, a reductant, a fuel and so on, and recently it has attracted much attention as a clean energy for our daily life since it exhausts just water when we use it, which is environment-friendly. Currently, most of hydrogen is produced through an industrial process from natural gas, i.e., steam reforming of methane (SRM) [1]. The process consists of multiple catalytic reactions and the entire chemical equation can be shown as Eq.1 [2].

$$CH_4 + 2\,H_2O \rightarrow 4\,H_2 + CO_2 \qquad \Delta G^{\ominus}_{298K} = 113.5\ \text{kJ mol}^{-1} \qquad (1)$$

The highly endergonic property of the reaction requires high reaction temperature, typically more than 1073 K, even in the presence of practical catalysts [2]. The high temperature operation causes several problems such as the large energy consumption, the unfavorable carbon formation, and the necessity of expensive reactor [3]. Thus, lowering the operation temperature has been highly desired in SRM. In order to decrease the reaction temperature and utilize sustainable solar energy, heterogeneous photocatalysis has been proposed for SRM as one of possible methods since photocatalysis can take place even at a lower temperature under photoirradiation [4–9].

We discovered platinum-loaded semiconductor photocatalysts, such as Pt/TiO_2 and Pt/$NaTaO_3$:La, can continuously promote photocatalytic steam reforming of methane (PSRM) around room temperature [10–12], and developed several kinds of metal loaded photocatalyst such as Pt/$CaTiO_3$ [13,14], Pt/Ga_2O_3 [15–17], and Rh/$K_2Ti_6O_{13}$ [18,19]. Among these studies, it is demonstrated that the photocatalytic activity can be improved by doping suitable amount of a certain metal cation to the semiconductor, e.g., La^{3+} to $NaTaO_3$ [10,12] and Mg^{2+} or Zn^{2+} to Ga_2O_3 [15,16]. Recently, it was found that fine and regularly shaped crystals of photocatalyst such as $NaTaO_3$ [20] and $Na_2Ti_6O_{13}$ [21]

prepared by a flux method exhibits higher activity in PSRM than untailored particles prepared by a conventional solid state reaction method. In the present study, we examined a flux method and La^{3+}-doping to improve the photocatalytic activity of $Pt/CaTiO_3$ photocatalyst. We synthesized several doped and non-doped $CaTiO_3$ photocatalysts by a flux method with various conditions and a conventional solid state reaction method, characterized them in several methods, and evaluated them in PSRM.

2. Experimental

2.1 Catalyst preparation

A series of La-doped $CaTiO_3$ compounds (denoted as CTO:La hereafter) were synthesized by a flux method and a solid state reaction method. The starting materials, $CaCO_3$ (Rare Metallic, 99.9%), TiO_2 (rutile, Kojundo, 99.9%), and La_2O_3 (Kishida, 99.99%) were mixed with a flux, such as NaCl (Kishida, 99.5%), KCl (Kishida, 99.5%), and $CaCl_2$ (Kishida, 95.0%): The molar ratio of $CaCO_3$, TiO_2, and La_2O_3 was $(100-x)$: 100 : $x/2$, where x showed the aimed doping amount of La (x = 0, 0.5, 1, 2, 3 and 5 mol%), and various concentration (y) of the solute in the molten flux mixture (y = 5, 10, 30, 50, 70, and 90 mol%; typically 50 mol%) were examined, where y was defined as: y [mol%] = 100 × (amount of CTO:La [mol]) / (amount of CTO:La [mol] + amount of a flux [mol]). The mixture of the starting materials and the flux in an aluminum crucible covered by a lid was heated at a rate of 200 K h^{-1} to 1373 K in an electric furnace, held at this temperature for 10 h, and then cooled down to 973 K at a cooling rate of 100 K h^{-1}, followed by natural cooling to room temperature in the furnace. The obtained product was dispersed in hot ion-exchanged water (500 mL, 353 K) and filtrated with suction to remove the flux. The washing procedure was repeated three times, and then dried at 323

K overnight. These samples are referred to as CTO(*flux*, *y*) for non-doped samples like CTO(NaCl, 50), and CTO:La(*x*, *flux*, *y*) for La-doped samples, like CTO:La(0.5, KCl, 50).

Another sample was prepared by a solid state reaction (SS) method without using the flux, corresponding to *y*=100, without La doping. The starting mixture of $CaCO_3$ and TiO_2 was ground well, followed by calcination in the same manner. The sample is referred to as CTO(SS).

Platinum co-catalyst was loaded onto the prepared CTO and CTO:La samples by an impregnation method. The sample was soaked in an aqueous solution of H_2PtCl_6 (Wako, 99.9%), evaporated at 331 K to dryness in a rotary evaporator, and then calcined at 673 K for 2 h. The samples are referred to as Pt(*z*)/CTO:La(*x*, *F*, *y*), where *z*= indicates the loading amount of Pt (*z* = 0, 0.03, 0.05, 0.1, 0.15 and 0.2 wt%; typically 0.05 wt%).

2.2 Characterization

X-ray diffraction (XRD) measurement was carried out at room temperature with a Shimadzu Lab X XRD-6000 using Cu Kα radiation (40 kV, 30 mA). The angle was corrected according to a diffraction of Si powder mixed with each sample. The crystallite size was determined by Scherrer equation using the full width at half maximum (FWHM) of the diffraction line at 2θ=33.1° in the XRD patterns of $CaTiO_3$ only when the average crystallite size over the limit of the application of Scherrer equation such as 100-200 nm [22].

Images of scanning electron microscopy (SEM) were taken by a JEOL JSM-890. Diffuse reflectance (DR) UV-visible spectrum was recorded on a JASCO V-670 equipped with an integrating sphere covered with a $BaSO_4$ reference. The band gap was estimated from the spectrum according to Tauc plot. The BET specific surface area was estimated

from the amount of N_2 adsorption at 77 K measured using a Quantachrome Monosorb MS-21.

X-ray absorption fine structure (XAFS) at La K-edge were recorded using a Si(311) monochromator in a transmission mode at NW-10A [23] of Photon Factory, Institute of Material Structure Science, High Energy Accelerator Research Organization (KEK-PF), Tsukuba, Japan. X-ray photoelectron spectroscopy (XPS) measurements were acquired using an X-ray photoelectron spectrometer (ESCA 3400, Shimadzu Corp.).

2.3 Photocatalytic activity tests

Photocatalytic reaction tests for the PSRM were carried out with a fixed-bed flow reactor as described in our previous studies [20,21]. The catalyst powder was pressed under 20 MPa for 1 min and ground into granules of 300–600 μm. The catalyst granules (0.7–0.8 g) were put into a quartz reactor (ca. 50 × 20 × 1 mm^3), where the irradiation area was regulated to be 6.0 cm^2 [21]. The reaction gas mixture composed of 25% CH_4 and 0.75% H_2O with an argon carrier was introduced at a flow rate of 15 mL min^{-1} at atmospheric pressure under light shielding condition for 30 min, and then the catalyst cell was irradiated from a 300 W xenon lamp without using any optical filter, where the light intensity was 25 mW cm^{-2} measured in the range of 254±10 nm. The temperature was measured to be around 323 K. The outlet gas was analyzed by online gas chromatography with a thermal conductivity detector at an interval of ca. 30 min. Since the sensitivity for CO_2 in the argon carrier was low, the experimental error for the values of CO_2 production rate was relatively large.

3. Results and discussion

3.1 Non-doped CTO samples prepared by a flux method with various fluxes.

The effects of a flux method and the kind of flux were studied before an examination of the doping effect. First, several $CaTiO_3$ samples were prepared by a flux method using various fluxes with the same solute concentration of 50%, and by a SS method. Fig. 1 shows the XRD patterns of these samples. From the diffraction patterns in the wide range (Fig. 1A), the crystal structure of these samples can be assigned to the orthorhombic perovskite $CaTiO_3$. In Fig. 1B, the diffraction line at 69.5° of these samples are shown. For the CTO(NaCl, 50) sample prepared by using a NaCl flux, a slight shift to the low angle side was observed (Fig. 1Ba). The ionic radius of Na^+ ions (1.39 Å when the coordination number (CN) is 12) contained in the flux is larger than that of Ca^{2+} ions (1.34 Å, CN=12), suggesting that Na^+ ions partially substituted for Ca^{2+} ions at the A-site of the perovskite structure. The CTO(KCl, 50) sample prepared using a KCl flux exhibited no shift (Fig. 1Bb), indicating that K^+ ions (1.64 Å, CN=12) were not substituted for Ca^{2+}. In addition, the width of the diffraction line was slightly larger than that of the CTO(SS) sample prepared by the SS method. This means that the sample prepared using the KCl flux consisted of smaller crystallites compared to the sample prepared by the SS method, which is consistent with the SEM image as mentioned later (Fig. 2). For the CTO($CaCl_2$, 50) sample prepared using a $CaCl_2$ flux, the diffraction line was slightly shifted to the higher angle (Fig. 1Bc). This shift to higher angle was observed only when the $CaCl_2$ flux was used. Since the ionic radius of Al^{3+} ion (0.54 Å, CN=6) is smaller than that of Ti^{4+} ion (0.605 Å, CN=6), it is suggested that Al^{3+} ions from the alumina crucible partially substituted for Ti^{4+} ions at the B-site of the perovskite structure [24]. This would be due to high solubility of Al_2O_3 in the $CaCl_2$ flux, since Al_2O_3 can be

dissolved in a molten $CaCl_2$, which can be applied to electrochemical aluminum metal production [25], but not in molten NaCl and KCl fluxes [26].

SEM images of these CTO samples are shown in Fig. 2. The particles of the sample prepared by the SS method exhibited irregular shape of ca. 0.54 μm on an average size. The samples prepared by the flux method consisted of particles with rather characteristic shapes, which would be regulated by the employed molten salts. The CTO(NaCl, 50) and CTO(KCl, 50) samples showed polyhedral particles, where some facets were found on the surface and the average sizes were ca. 0.43 and 0.60 μm, respectively. The $CaCl_2$ flux gave well-regulated cubic or rectangular crystals of larger size like ca. 9 μm, which is obviously larger than the particles of other samples, which is consistent with the smaller BET specific surface area (Table 1). In general, a flux can contribute to fabricate well-defined crystals covered with facets. In this method, since supersaturation with decreasing temperature or evaporation of flux would be major driving forces for crystallization, the solubility of the materials would be an important factor. It is known that the presence of common anion or cation in the flux often increase the solubility of substrate [27,28]. Thus, the solubility of the Ca^{2+} cation from the start material in the $CaCl_2$ flux is considered to be higher than that in the other fluxes [25,26]. As a result, the $CaCl_2$ flux would enhance the crystal growth of $CaTiO_3$.

In the DR UV-visible spectra (Fig. 3), the CTO(NaCl, 50), CTO(KCl, 50), and CTO(SS) samples exhibited the absorption edge around 350 nm in wavelength and the estimated band gap was 3.5 eV. The CTO(SS) sample showed additionally a small shoulder near the absorption edge at 350–400 nm in wavelength. Although no impurity phase was observed in the XRD pattern (Fig. 1), this shoulder would be assigned to amorphous-like TiO_2, although the other possibilities such as crystal defects could not be

excluded. This small absorption has been observed for $CaTiO_3$ samples prepared by solid state reaction methods in our previous studies [13,29,30]. The CTO($CaCl_2$, 50) sample exhibited a red-shifted threshold at 360 nm, corresponding to 3.4 eV, and also the similar band around absorption edge as well as a broad absorption band in the visible light region of 400–800 nm. The latter wide absorption band would derive from defects such as color centers [31] or Al^{3+} impurity from alumina crucible as discussed above [24]. The substitution of Al^{3+} for Ti^{4+} at the B-site would form residual amorphous-like TiO_2 species showing the former band around absorption edge.

The photocatalytic reaction tests were carried out for these samples, on which 0.05 wt% of Pt cocatalyst was deposited before the reaction test. Fig. 4 shows a time course of the production rate of H_2 and CO_2 as well as these ratio (H_2/CO_2) in the photocatalytic reaction test with the Pt(0.05)/CTO(KCl, 50) sample as a representative. Without photoirradiation, no products were observed. Upon photoirradiation, although the production rates of H_2 and CO_2 initially varied with time, both of them became constant after 2 h, and the formation ratio also became stable around 4. These results suggest that the PSRM proceeded as expected according to the Eq. 1.

Fig. 5 shows the H_2 production rates in the PSRM with the Pt(0.05)/CTO catalysts. The Pt(0.05)/CTO(KCl, 50) sample prepared by the flux method with a KCl flux exhibited the highest production rate among them, which was 3.3 times higher than the Pt(0.05)/CTO(SS) sample prepared by the conventional SS method. The Pt(0.05)/CTO(NaCl, 50) and Pt(0.05)/CTO($CaCl_2$, 50) samples exhibited lower production rates than the Pt(0.05)/CTO(SS) sample.

The H_2 production rate with these photocatalysts are listed in Table 1 entries 1–4, in which particle size determined from SEM images and specific surface area of these

samples are also listed. Although no clear relationship was found between particle size and H_2 production rate, the sample with larger specific surface area tended to show higher photocatalytic activity among them. However, as discussed later, this trend cannot be always found, indicating there are some structural factors controlling the photocatalytic activity and the most important factor cannot be determined easily. The results of characterization revealed that the Pt(0.05)/CTO(KCl, 50) sample had fine polyhedral crystals with less impurities substituted and a larger specific surface area. It was proposed that less impurities and the larger specific surface area would contribute to the improvement of the activity.

As a conclusion of this section, the sample prepared with a KCl flux can exhibit the highest photocatalytic performance in PSRM. Thus, we focused further investigation on the samples prepared with the KCl flux.

3.2. Non-doped CTO samples prepared with various solute concentrations.

In the XRD patterns of the CTO(KCl, *y*) samples prepared using a KCl flux with different solute concentration (*y* mol%) and the CTO(SS) sample (Fig. S1, in Supplementary information), all the samples presented clear diffraction lines assignable to $CaTiO_3$ crystal without any impurity phase and any shift. SEM images revealed that the CTO(KCl, *y*) samples consisted of polyhedral particles of 0.4–0.6 μm in size (Fig. S2 and Table 1 entries, 2 and 5–9). It was found that a moderate concentration of the solutes such as 50% gave the largest particle size such as 0.6 μm determined by the SEM images. Fig. S3 shows DR UV-visible spectra. All the samples had an absorption edge around 350 nm. The CTO(KCl, 10) sample showed less absorption at 350–400 nm than others. The sample with larger solute concentration exhibited the broad absorption band in 400–800

nm, suggesting that the CTO(KCl, *y*) samples prepared using a larger amount of KCl flux tends to have less defects. Since a flux acts as a solvent for crystallization of the aimed material [27,28], small amount of flux (90% of solute) would not enough for the complete crystallization. A moderate amount of flux would provide a suitable concentrations of the starting materials and enough space to achieve a homogenous dispersion of the formed particles, which would enhance the crystal growth to give larger size of well-crystallized particles covered with well-defined facets. The moderate amount of flux would be 50% to fabricate the fine $CaTiO_3$ crystals in the present conditions.

Fig. 6A shows the hydrogen production rates in the PSRM with the Pt(0.05)/CTO(KCl, *y*) photocatalysts using the KCl flux with different solute concentration (*y* mol%). The H_2 production rate increased with increasing the solute concentration up to 50 mol%. The sample prepared with a solute concentration of 50 mol% in a molten mixture gave the highest production rate such as 12 μmol h^{-1} among them. However, higher solute concentrations than 50 mol% decreased the photocatalytic activity. As mentioned above, the CTO(KCl, 50) samples had large size of well-crystallized polyhedral particles with less defects, which would contribute to the highest activity among these samples. This is consistent with the previous studies of $NaTaO_3$ [20] and $Na_2Ti_6O_{13}$ [21] photocatalysts prepared via a flux method for PSRM, where the photocatalyst prepared with a moderate solute concentration gave the highest activity.

Fig. 6B shows the hydrogen production rates with the Pt(*x*)/CTO(KCl, 50) photocatalysts of various Pt loading amount (*x* wt%). The Pt(0.05)/CTO(KCl, 50) sample exhibited the highest production rate among them. The samples with Pt loading amount lower and higher than 0.05 wt% exhibited lower photocatalytic activity, which is possibly caused by some reasons, such as an aggregation of the Pt species [32], an increase of

recombination sites [33], shielding light reaching photocatalyst [34], and varying the Pt fermi level [32].

So far we have investigated some photocatalyst systems for PSRM, such as $NaTaO_3$:La [20], $Na_2Ti_6O_{13}$ [21], and $CaTiO_3$ (This study), prepared by a flux method. In any cases, the samples prepared by a flux method exhibited higher activity than the samples prepared by a SS method (Table S1). The Pt/$NaTaO_3$:La photocatalyst prepared using a NaCl flux exhibited 1.6 times higher activity than the sample prepared by a SS method (Table S1 entries 2 and 3). The Rh/$Na_2Ti_6O_{13}$ photocatalyst prepared using a NaCl flux showed only 1.1 times higher activity than the sample prepared by a SS method (Table S1, entries 4 and 5). In the current Pt/$CaTiO_3$ photocatalyst prepared using a KCl flux showed 3.3 times higher activity than the sample prepared by a SS method. The flux method can be proposed as a superior method than the conventional solid state reaction method to provide an active photocatalyst for PSRM. The current $CaTiO_3$ photocatalyst was most improved by the flux method among the three photocatalyst systems mentioned above.

In conclusion of this section, the Pt(0.05)/CTO(KCl, 50) sample exhibited the highest activity, which would originate from the well-crystalized, large polyhedral $CaTiO_3$ crystals with less defects and less impurity, loaded with a moderate amount of Pt cocatalyst. Thus, we moved on the investigation of La doping effect on the photocatalyst.

3.3. La-doped CTO samples prepared by a KCl flux.

La-doped samples were prepared by using a KCl flux with various La doping amount. Fig. 7A shows the XRD patterns of the CTO:La(*x*, KCl, 50) samples with various La doping amount. The entire patterns were assignable to the $CaTiO_3$ perovskite structure

except for details. In Fig. 7B focuses a diffraction line at 69.5°. With increasing La doping amount from 0.5 to 5 mol%, the diffraction line shifted to lower angle. This suggests that La^{3+} (1.36 Å, CN=12) was doped into the $CaTiO_3$ lattice to substitute for Ca^{2+} (1.34 Å, CN=12) at the A-site in the perovskite ABO_3 structure by using the flux method. Since the ionic radius of the six-coordinated La^{3+} ion (1.032 Å, CN=6) is much larger than that of Ti^{4+} ion (0.605 A, CN=6) and the observed shift of the diffraction line was not so large, it is considered that La^{3+} could not substitute for Ti^{4+}.

When the La content was 0.5 mol% (Fig. 7b), the line intensities were higher and the widths were lower than those of non-doped sample, indicating the crystal growth with less strain was enhanced on the CTO:La(0.5, KCl, 50) sample. The CTO:La(1, KCl, 50) sample exhibited almost the same intensity and width as those of the non-doped CTO(KCl, 50) sample (Fig. 7c), suggesting that the substituted La are present without much influence on the crystal growth of $CaTiO_3$. With increasing La doping amount more than 1 mol%, the diffraction lines became weeker and broader, especially the line at 69.5° almost disappeared when 5 mol% La was doped, suggesting that the crystal structure were much varied. The substitution by La^{3+} cation having the slightly larger ionic radius and the higher valence than those of Ca^{2+} would distort the crystal structure, generate many crystal defects, and thus make the diffraction line broad and ambiguous.

Fig. 8 shows their SEM images. The polyhedral morphology was not so changed by La doping. However, the particle size was drastically changed by La doping as listed in Table 1, entries 10–15 and plotted in Fig. 9. The particle size drastically increased by the La doping when the amount of La was less than 1 mol% (Fig. 8b and Table 1, entries 10–12). The maximum particle size was 1.4 μm on an average for the CTO:La(0.5, KCl, 50) sample (Table 1 entry 11), which was 2.3 times larger than that of the non-doped

CTO(KCl, 50) sample (Table 1, entry 2). Similar observations of this characteristic crystal growth have been reported, e.g., for $SrTiO_3$ doped with Y^{3+}, La^{3+}, Nd^{3+}, Ho^{3+}, Nb^{5+}, and Sb^{5+} [35–37], which is well-known as an anomaly of grain growth of donor-doped perovskite materials, so-called “donor anomaly”[36], the mechanism of which has been thermodynamically explained [38]. Except for the samples with low La doping amount less than 1 mol%, the particle size tends to decrease with the increase of the doping amount in the range of 1–5 mol% (Fig. 9). This means that small amount of La cations enhanced the anomalous crystal growth of $CaTiO_3$ in the molten flux, while larger amount of La suppressed it.

Fig. 10 shows the DR UV-visible spectra of the CTO:La(*x*, KCl, 50) samples with various La doping amount (0–5 mol%). All the samples exhibited the same threshold at 350 nm in wavelength, corresponding to the bandgap of 3.5 eV. The non-doped sample exhibited a band at 350–400 nm and a very small and broad band centered at 500 nm (Fig. 10a). The both bands were suppressed by doping 0.5 mol% La, suggesting that La doping suppresses the formation of defects in $CaTiO_3$ crystals. Further doping of La more than 1 mol% increased the band at 350–400 nm without showing another broad band at 500 nm.

To elucidate the state of the doped La ions, XAFS spectra were measured and analyzed. XANES spectra of the CTO:La(*x*, KCl, 50) samples are resemble to that of La_2O_3 (Fig. 11A), because of the less characteristic feature of La K-edge XANES at high energy of incident X-ray such as 39 keV and unchangeable valence of La^{3+} cation. The EXAFS oscillations of the all CTO:La samples (Fig. 11B, a–d), were clearly different from that of La_2O_3 (Fig. 11B, e), indicating the local structure of major La^{3+} ions in the CTO:La(*x*, KCl, 50) samples, with x=0.5, 1, 3, and 5 mol %, are quite different from that in the trigonal structure of La_2O_3. In the Fourier Transformed EXAFS of the CTO:La(*x*,

KCl, 50) samples (Fig. 11C, a–d), the first and the second neighboring atoms were clearly observed around at 1.9 and 2.9 Å, respectively, which were clearly different from and closer than that of La_2O_3 (Fig. 11C, e) and similar to the reported one for a $NaTaO_3$:La(La 0.5 mol%) photocatalyst [12]. It is clear that the local structure of La^{3+} cation in each CTO:La sample with doping amount of 0.5–5 mol% was similar to each other and different from that in La_2O_3 crystal, supporting that La^{3+} cation substituted for the Ca^{2+} cation in the $CaTiO_3$ structure. Thus, the absorbing La^{3+} ions are located at the A-site in ABO_3 perovskite structure and are coordinated with twelve O^{2-} anions and surrounded by eight Ti^{4+} cations at the B-site, which would correspond to the peaks at 1.9 and 2.9 Å, respectively. It was also confirmed that the average local structure of La was not varied so much with the La contents in these samples.

Fig. 12 shows XPS spectra of La 3d bands for the CTO:La(*x*, KCl, 50) samples and La_2O_3. The $3d_{5/2}$ and $3d_{3/2}$ bands observed at 835 and 852 eV, respectively, were accompanied with each satellite band at higher binding energy side, which are assigned to charge-transfer satellite bands from neighboring oxygen to the La [39]. The shapes of $3d_{5/2}$ and $3d_{3/2}$ bands of the CTO:La(0.5, KCl, 50) sample (Fig. 12a) were quite different from those of La_2O_3 (Fig. 12d), *i.e.*, the satellite bands were relatively larger than those of La_2O_3. This means that La^{3+} ions in the $CaTiO_3$ structure had a unique electronic state that is different from those in the bulk oxide of La_2O_3 because of larger interaction with surrounding oxygen anions. As shown in the Fourier transformed EXAFS (Fig. 11C), the distances between La^{3+} cation and neighboring oxygen anions in the $CaTiO_3$ lattice, are shorter than those in La_2O_3, which is consistent with the relatively larger satellite bands. Thus, it is suggested that the La^{3+} cation substituted for Ca^{2+} cation would provide larger interaction with oxygen anions. In contrast, a similar band shape to that of La_2O_3 was

found for the CTO:La(5, KCl, 50) sample (Fig. 12c), meaning the La^{3+} ions in the highly La-doped sample are rather similar electronic state with that in the bulk La_2O_3. As mentioned above, the EXAFS analysis (Fig. 11C) clarified that the La^{3+} cation in the samples substituted Ca^{2+} cation in the $CaTiO_3$ structure. The ambiguous X-ray diffraction line (Fig. 7Be) means that the perovskite structure of $CaTiO_3$ was much influenced by the 5 mol% La doping. These facts propose that the large amount of La^{3+} cations was substituted for Ca^{2+} cations in the $CaTiO_3$ crystal and they have the similar electronic state of La^{3+} cations to that of La_2O_3. The CTO:La(1, KCl, 50) sample exhibited similar band shape to the low doping sample but also showed slightly similar character to the high doping sample.

Finally, the photocatalytic activity test in PSRM were carried out for the Pt-loaded La-doped $CaTiO_3$ photocatalysts with various lanthanum doping amounts (Table 1, entries 10–15). Fig. 13 depicts the hydrogen production rate over the Pt(0.05)/CTO:La(*x*, KCl, 50) samples and non-doped Pt(0.05)/CTO(KCl, 50) sample. Among them, the Pt(0.05)/CTO:La(1, KCl, 50) sample exhibited the highest H_2 production rate such as 19 μmol h^{-1}, which was 1.6 times larger than non-doped Pt(0.05)/CTO:La(KCl, 50) sample and the best performance in the present study. The low amount of La-doping less than 1 mol% drastically decreased the photocatalytic activity such as one fifth of that with the non-doped sample. For the higher amount of La-doping more than 1 mol%, the photocatalytic activity decreased with an increase of La-doping amount.

The photocatalytic activity should be related to the structural properties. At least, it was clarified that the defects showing the absorption bands in visible light region decrease the photocatalytic activity. However, other structural properties could not simply

explain the photocatalytic activity. The large size of the particles with a low specific surface area according to anomalous crystal growth by small amount of La doping less than 1 mol% exhibited low activity (Table 1 entries 10–12). The variation of the specific surface area could not quantitatively explain the variation of the photocatalytic activity. In the photocatalyst crystal, only the photogenerated electrons and holes reaching the surface without recombination can take part in the photocatalytic reaction, and thus the crystal edges providing both the reductive and oxidative reaction fields would decrease the recombination to increase the photocatalytic activity [40]. Thus, a large crystal having less edges would show less activity. The higher amount of La-doping more than 1 mol% decreased the crystal size and the photocatalytic activity with an increase of La-doping amount (Table 1, entries 13–15). As one possibility, since these samples would be of low crystallinity judging from the ambiguous x-ray diffraction lines, these samples might have many crystal defects that cannot be detected by DR UV-vis spectra and these defects would act as the recombination sites for the photoexcited electrons and holes.

4. CONCLUSIONS

In the present study, the fine polyhedral $CaTiO_3$ (CTO) crystals were synthesized by a flux method and a conventional solid state reaction (SS) method for an application to the photocatalytic steam reforming of methane (PSRM). The type of fluxes and the solute concentration in the molten mixture much affected the structure of the CTO crystals, such as crystal shape, crystal size, crystallinity, specific surface area, and amount of defects. The Pt-loaded sample prepared using a KCl flux showed 3.3 times higher H_2 production rate than the sample prepared by the conventional SS method.

Furthermore, the lanthanum doped CTO photocatalysts (CTO:La) were prepared by the flux method using a KCl flux. La cation was successfully doped at the Ca site in the $CaTiO_3$ lattice. The addition of La in small amount induced the crystal growth of the CTO, but larger amount of La suppressed the growth. The sample with a moderate amount of La, Pt(0.05)/CTO:La(1, KCl, 50), exhibited the highest H_2 formation rate in the present study, which was 1.6 times higher than the non-doped sample prepared by the flux method, Pt(0.05)/CTO(KCl, 50), and 5.3 times higher than non-doped sample prepared by the solid state reaction method, Pt(0.05)/CTO(SS).

The relationship between the photocatalytic activity and the structural properties was discussed. At least, it was clarified that the defects giving rise to the absorption bands in visible light region decreased the photocatalytic activity. However, other structural properties could not simply explain the photocatalytic activity.

ACKNOWLEDGMENT

The authors acknowledge the kindness of S. Kikkawa, Prof. K. Teramura, and Prof. T. Tanaka at Kyoto University for helping the XPS measurement. The XAFS measurements were performed under the approval of the Photon Factory Program Advisory Committee (Proposal No. 2016G643 and 2018G625). This work was partially supported by a Grant-in-Aid for Scientific Research (B), (25289285), and a Grant-in-Aid for Scientific Research on Innovative Areas “Artificial photosynthesis (AnApple)” (25107515) and “Singularity” (17H05334) from the Japan Society for the Promotion of Science (JSPS).

REFERENCES

[1] D. Das, T.N. Veziroglu, Hydrogen production by biological processes: a survey of literature, Int. J. Hydrogen Energy. 26 (2001) 13–28. doi:10.1016/S0360-3199(00)00058-6.

[2] L. Barelli, G. Bidini, F. Gallorini, S. Servili, Hydrogen production through sorption-enhanced steam methane reforming and membrane technology: A review, Energy. 33 (2008) 554–570. doi:10.1016/j.energy.2007.10.018.

[3] J. Tong, Y. Matsumura, Effect of catalytic activity on methane steam reforming in hydrogen-permeable membrane reactor, Appl. Catal. A Gen. 286 (2005) 226–231. doi:10.1016/j.apcata.2005.03.013.

[4] L. Yuliati, H. Yoshida, Photocatalytic conversion of methane., Chem. Soc. Rev. 37 (2008) 1592–1602. doi:10.1039/b710575b.

[5] K. Shimura, H. Yoshida, Heterogeneous photocatalytic hydrogen production from water and biomass derivatives, Energy Environ. Sci. 4 (2011) 2467–2481. doi:10.1039/c1ee01120k.

[6] K. Shimura, H. Yoshida, Semiconductor photocatalysts for non-oxidative coupling, dry reforming and steam reforming of methane, Catal. Surv. from Asia. 18 (2014) 24–33. doi:10.1007/s10563-014-9165-z.

[7] H. Song, X. Meng, Z.J. Wang, Z. Wang, H. Chen, Y. Weng, F. Ichihara, M. Oshikiri, T. Kako, J. Ye, Visible-light-mediated methane activation for steam methane reforming under mild conditions: A case study of Rh/TiO2 catalysts, ACS Catal. 8 (2018) 7556–7565. doi:10.1021/acscatal.8b01787.

[8] A.M. Pennington, R.A. Yang, D.T. Munoz, F.E. Celik, Metal-free hydrogen evolution over defect-rich anatase titanium dioxide, Int. J. Hydrogen Energy. 43 (2018) 15176–15190. doi:10.1016/j.ijhydene.2018.06.096.

[9] B. Han, W. Wei, M. Li, K. Sun, Y.H. Hu, A thermo-photo hybrid process for steam reforming of methane: highly efficient visible light photocatalysis, Chem. Commun. (2019) in press. doi:10.1039/C9CC04193A.

[10] H. Yoshida, S. Kato, K. Hirao, J.-I. Nishimoto, T. Hattori, Photocatalytic steam reforming of methane over platinum-loaded semiconductors for hydrogen production, Chem. Lett. 36 (2007) 430–431. doi:10.1246/cl.2007.430.

[11] H. Yoshida, K. Hirao, J.-I. Nishimoto, K. Shimura, S. Kato, H. Itoh, T. Hattori, Hydrogen production from methane and water on platinum loaded titanium oxide photocatalysts, J. Phys. Chem. C. 112 (2008) 5542–5551. doi:10.1021/jp077314u.

[12] K. Shimura, S. Kato, T. Yoshida, H. Itoh, T. Hattori, H. Yoshida, Photocatalytic steam reforming of methane over sodium tantalate, J. Phys. Chem. C. 114 (2010) 3493–3503. doi:10.1021/jp902761x.

[13] K. Shimura, H. Miyanaga, H. Yoshida, Preparation of calcium titanate photocatalysts for hydrogen production, Stud. Surf. Sci. Catal. 175 (2010) 85–92. doi:10.1016/S0167-2991(10)75011-4.

[14] K. Shimura, H. Yoshida, Hydrogen production from water and methane over Pt-loaded calcium titanate photocatalyst, Energy Environ. Sci. 3 (2010) 615. doi:10.1039/b922793h.

[15] K. Shimura, T. Yoshida, H. Yoshida, Photocatalytic activation of water and methane over modified gallium oxide for hydrogen production, J. Phys. Chem. C. 114 (2010) 11466–11474. doi:10.1021/jp1012126.

[16] K. Shimura, H. Yoshida, Effect of doped zinc species on the photocatalytic activity of gallium oxide for hydrogen production, Phys. Chem. Chem. Phys. 14 (2012) 2678–2684. doi:10.1039/c2cp23220k.

[17] K. Shimura, K. Maeda, H. Yoshida, Thermal Acceleration of Electron Migration in Gallium Oxide Photocatalysts, J. Phys. Chem. C. 115 (2011) 9041–9047. doi:10.1021/jp110824n.

[18] K. Shimura, H. Kawai, T. Yoshida, H. Yoshida, Simultaneously photodeposited rhodium metal and oxide nanoparticles promoting photocatalytic hydrogen production, Chem. Commun. 47 (2011) 8958–8960. doi:10.1039/c1cc12287h.

[19] K. Shimura, H. Kawai, T. Yoshida, H. Yoshida, Bifunctional rhodium cocatalysts for photocatalytic steam reforming of methane over alkaline titanate, ACS Catal. 2 (2012) 2126–2134. doi:10.1021/cs2006229.

[20] A. Yamamoto, S. Mizuba, Y. Saeki, H. Yoshida, Platinum loaded sodium tantalate photocatalysts prepared by a flux method for photocatalytic steam reforming of methane, Appl. Catal. A Gen. 521 (2016) 125–132. doi:10.1016/j.apcata.2015.10.031.

[21] H. Yoshida, S. Mizuba, A. Yamamoto, Preparation of sodium hexatitanate photocatalysts by a flux method for photocatalytic steam reforming of methane, Catal. Today. 334 (2019) 30–36. doi:10.1016/j.cattod.2019.02.055.

[22] U. Holzwarth, N. Gibson, The Scherrer equation versus the “Debye-Scherrer equation,” Nat. Nanotechnol. 6 (2011) 534–534. doi:10.1038/nnano.2011.145.

[23] M. Nomura, Y. Koike, M. Sato, A. Koyama, Y. Inada, K. Asakura, A new XAFS beamline NW10A at the photon factory, AIP Conf. Proc. 882 (2007) 896–898. doi:10.1063/1.2644697.

[24] Y. Ham, T. Hisatomi, Y. Goto, Y. Moriya, Y. Sakata, A. Yamakata, J. Kubota, K. Domen, Flux-mediated doping of SrTiO3 photocatalysts for efficient overall water splitting, J. Mater. Chem. A. 4 (2016) 3027–3033. doi:10.1039/c5ta04843e.

[25] H. Kadowaki, Y. Katasho, K. Yasuda, T. Nohira, Electrolytic reduction of solid Al2O3 to liquid Al in molten CaCl2, J. Electrochem. Soc. 165 (2018) D83–D89. doi:10.1149/2.1191802jes.

[26] Y. Xiao, K. Tang, Solubility of Alumina in Molten Chloride-Fluoride Melts, in: Proc. VIII Int. Conf. Molten Slags, Fluxes Salts, 2009: pp. 1393–1401.

[27] D.E. Bugaris, H.C. Zur Loye, Materials discovery by flux crystal growth: Quaternary and higher order oxides, Angew. Chemie - Int. Ed. 51 (2012) 3780–3811. doi:10.1002/anie.201102676.

[28] K.H. Yoon, Y.S. Cho, D.H. Kang, Molten salt synthesis of lead-based relaxors, J. Mater. Sci. 33 (1998) 2977–2984. doi:10.1023/A:1004310931643.

[29] H. Yoshida, R. Yamada, T. Yoshida, Platinum cocatalyst loaded on calcium titanate photocatalyst for water splitting in a flow of water vapor, ChemSusChem. 12 (2019) 1958–1965. doi:10.1002/cssc.201802799.

[30] H. Yoshida, L. Zhang, M. Sato, T. Morikawa, T. Kajino, T. Sekito, S. Matsumoto, H. Hirata, Calcium titanate photocatalyst prepared by a flux method for reduction of carbon dioxide with water, Catal. Today. 251 (2015) 132–139. doi:10.1016/j.cattod.2014.10.039.

[31] K. Lehovec, G.A. Shirn, Conductivity injection and extraction in polycrystalline barium titanate, J. Appl. Phys. 33 (1962) 2036–2044. doi:10.1063/1.1728890.

[32] H. Yuzawa, T. Mori, H. Itoh, H. Yoshida, Reaction mechanism of ammonia decomposition to nitrogen and hydrogen over metal loaded titanium oxide photocatalyst, J. Phys. Chem. C. 116 (2012) 4126–4136. doi:10.1021/jp209795t.

[33] K. Wang, Z. Wei, B. Ohtani, E. Kowalska, Interparticle electron transfer in methanol dehydrogenation on platinum-loaded titania particles prepared from P25,

Catal. Today. 303 (2018) 327–333. doi:10.1016/j.cattod.2017.08.046.

[34] N. Bao, L. Shen, T. Takata, K. Domen, Self-templated synthesis of nanoporous CdS nanostructures for highly efficient photocatalytic hydrogen production under visible light, Chem. Mater. 20 (2008) 110–117. doi:10.1021/cm7029344.

[35] I. Burn, S. Neirman, Dielectric properties of donor-doped polycrystalline SrTiO3, J. Mater. Sci. 17 (1982) 3510–3524. doi:10.1007/BF00752196.

[36] C. Peng, Y. Chiang, Grain growth in donor-doped SrTiO 3, J. Mater. Res. 5 (1990) 1237–1245.

[37] S. Hui, A. Petric, Evaluation of yttrium-doped SrTiO3 as an anode for solid oxide fuel cells, J. Eur. Ceram. Soc. 22 (2002) 1673–1681. doi:10.1016/S0955-2219(01)00485-X.

[38] M. Drofenik, Origin of the Grain Growth Anomaly in Donor-Doped Barium Titanate, J. Am. Ceram. Soc. 76 (1993) 123–128. doi:10.1111/j.1151-2916.1993.tb03697.x.

[39] G. Crecelius, G.K. Wertheim, D.N.E. Buchanan, Core-hole screening in lanthanide metals, Phys. Rev. B. 18 (1978) 6519–6524. doi:10.1103/PhysRevB.18.6519.

[40] H. Kato, K. Asakura, A. Kudo, Highly efficient water splitting into H2 and O2 over lanthanum-doped NaTaO3 photocatalysts with high crystallinity and surface nanostructure, J. Am. Chem. Soc. 125 (2003) 3082–3089. doi:10.1021/ja027751g.

LIST OF TABLE AND FIGURES.

Table 1 Physical and optical properties of the $CaTiO_3$:La samples prepared by the flux method and the photocatalytic property of the Pt(0.05)/$CaTiO_3$:La samples in the photocatalytic steam reforming of methane.

Fig. 1. XRD patterns of the CTO(flux, 50) samples, (a) CTO(NaCl, 50), (b) CTO(KCl, 50), and (c) CTO(CaCl2, 50), and (d) the CTO(SS) sample. The angle was corrected according to a diffraction of Si powder mixed with each sample.

Fig. 2. SEM images of the CTO(*flux*, 50) samples, (a) CTO(NaCl, 50), (b) CTO(KCl, 50), and (c) CTO($CaCl_2$, 50), and (d) the CTO(SS) sample.

Fig. 3. DR UV-visible spectra of the CTO(*flux*, 50) samples, (a) CTO(NaCl, 50), (b) CTO(KCl, 50), and (c) CTO($CaCl_2$, 50), and (d) the CTO(SS) sample.

Fig. 4. Time course of the production rates of (a) H_2 and (b) CO_2 (left), and (c) the ratio of H_2/CO_2 (right) in the photocatalytic reaction test with Pt(0.05)/CTO(KCl, 50) sample.

Fig. 5. Hydrogen production rate in PSRM with the Pt(0.05)/CTO(*flux*, 50) samples, (a) Pt(0.05)/CTO(NaCl, 50), (b) Pt(0.05)/CTO(KCl, 50), and (c) Pt(0.05)/CTO($CaCl_2$, 50), and (d) the Pt(0.05)/CTO(SS) sample.

Fig. 6. Hydrogen production rate in PSRM with (A) the Pt(0.05)/CTO(KCl, *y*) samples prepared by a flux method with various solute concentration (*y* mol%) in a KCl flux, and (B) the Pt(*x*)/CTO(KCl, 50) samples of various Pt loading amount (*x* wt%).

Fig. 7. XRD patterns of the CTO:La(*x*, KCl, 50) samples in the range of (A) 10°–80° and (B) 69°–70°, where La doping amount *x* was (a) 0, (b) 0.5, (c) 1, (d) 3, and (e) 5 mol %, and (f) La_2O_3 as a reference.

Fig. 8. SEM images of the CTO:La(*x*, KCl, 50) samples with different La doping amount *x*; (a) 0, (b) 0.5, (c) 1, (d) 3, and (e) 5 mol%.

Fig. 9. The average particle size determined from SEM images of the CTO:La(*x*, KCl, 50) samples with different La doping amount (*x* mol%).

Fig. 10. DR UV-visible spectra of the CTO:La(*x*, KCl, 50) samples with different La doping amount *x*; (a) 0, (b) 0.5, (c) 1, (d) 3, and (e) 5 mol %.

Fig. 11. (A) La K-edge XANES spectra, (B) EXAFS oscillations, and (C) Fourier transforms of the EXAFS oscillation for the CTO(*x*, KCl, 50) samples, where La doping amount *x* was (a) 0.5, (b) 1, (c) 3, and (d) 5 mol%, and (e) those for La_2O_3 as a reference.

Fig. 12. La 3d bands XPS spectra of the CTO(*x*, KCl, 50) samples with La doping amount x; (a) 0.5, (b) 1, and (c) 5 mol%, and (d) that of La_2O_3 as a reference.

Fig. 13. Hydrogen production rate in PSRM with the Pt(0.05)/CTO:La(*x*, KCl, 50) samples prepared by a flux method with various La contents (*x* mol %).

Table 1 Physical and optical properties of the $CaTiO_3$:La samples prepared by the flux method and the photocatalytic property of the Pt(0.05)/$CaTiO_3$:La samples in the photocatalytic steam reforming of methane.

Entry	Flux reagent	Solute concentration [a] (mol%)	La content (mol%)	Crystallite size (XRD) [b] / nm	Particle size (SEM) [c] / μm	S_{BET} [d] / m^2g^{-1}	H_2 production rate [e] / μmol h^{-1}
1	NaCl	50	0	– [f]	0.43	1.16	1.2
2	KCl	50	0	–	0.60	2.30	12
3	$CaCl_2$	50	0	–	9.0	0.35	1.2
4	(SS method)	100	0	–	0.54	1.58	3.6
5	KCl	10	0	–	0.37	2.54	1.2
6	KCl	30	0	–	0.38	2.75	1.2
8	KCl	70	0	–	0.4	2.22	5.4
9	KCl	90	0	–	0.47	2.11	7.8
10	KCl	50	0.1	–	1.1	1.37	4.2
11	KCl	50	0.5	–	1.4	0.92	2.4
12	KCl	50	0.7	–	1.1	1.41	6.6
13	KCl	50	1	–	0.45	1.85	19
14	KCl	50	3	36.2	0.21	4.40	14
15	KCl	50	5	30.5	0.2	4.73	6.0

[a] Solute concentration in the molten mixture. See the text for the calculation. [b] Average crystallite size of $CaTiO_3$ calculated from a line width at $2\theta=33.1°$ in the XRD patterns. [c] Average particle size of $CaTiO_3$ estimated from the SEM images. [d] Specific surface area obtained from the BET method. [e] The hydrogen production rate was evaluated at 3 h later from the start of photoirradiation. [f] Average crystallite size over the limit of the application of Scherrer equation such as 100–200 nm [22].

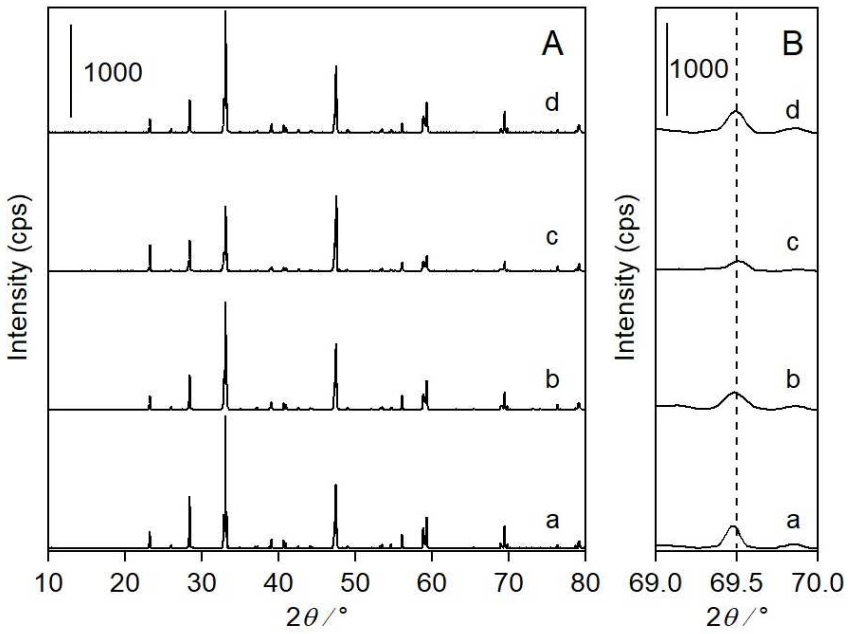

Fig. 1. XRD patterns of the CTO(*flux*, 50) samples, (a) CTO(NaCl, 50), (b) CTO(KCl, 50), and (c) CTO($CaCl_2$, 50), and (d) the CTO(SS) sample. The angle was corrected according to a diffraction of Si powder mixed with each sample.

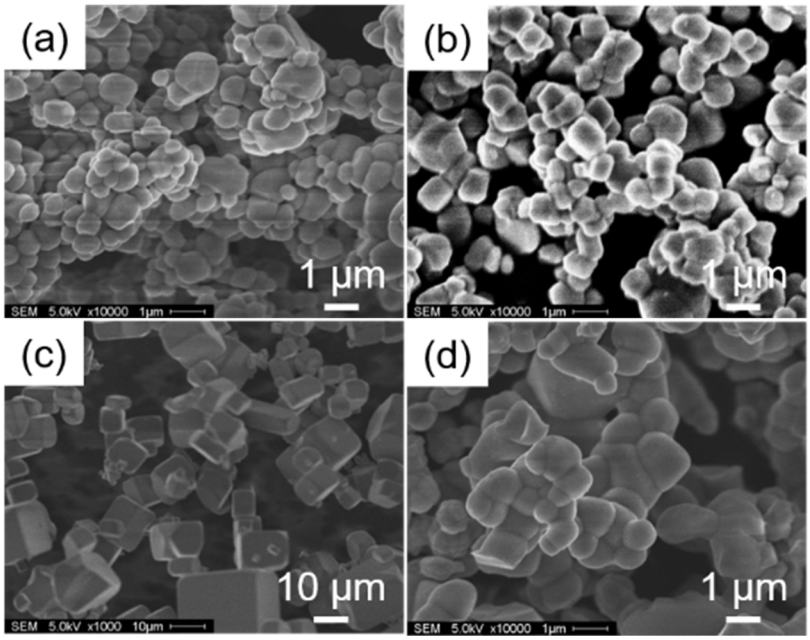

Fig. 2. SEM images of the CTO(*flux*, 50) samples, (a) CTO(NaCl, 50), (b) CTO(KCl, 50), and (c) CTO($CaCl_2$, 50), and (d) the CTO(SS) sample.

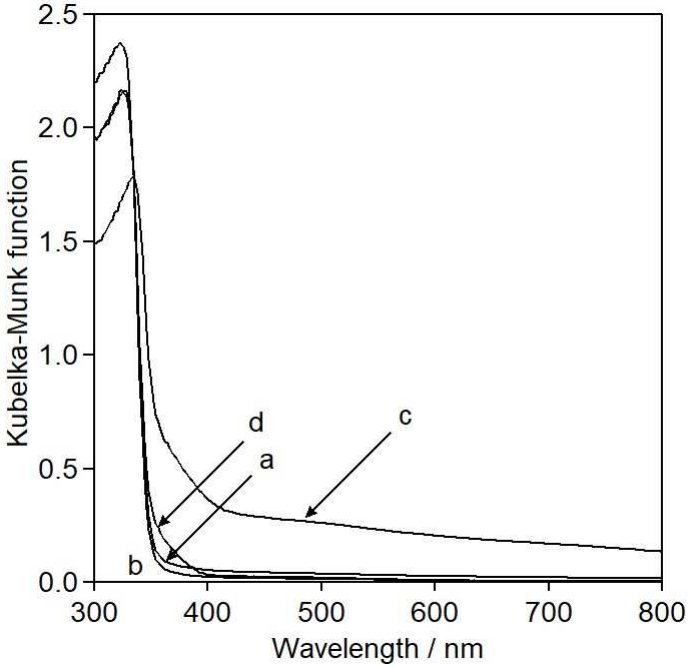

Fig. 3. DR UV-visible spectra of the CTO(*flux*, 50) samples, (a) CTO(NaCl, 50), (b) CTO(KCl, 50), and (c) CTO($CaCl_2$, 50), and (d) the CTO(SS) sample.

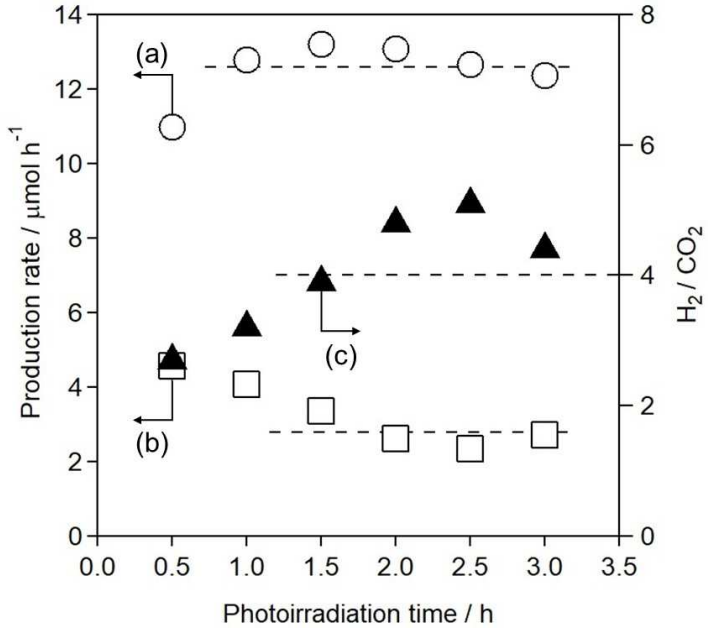

Fig. 4. Time course of the production rates of (a) H_2 and (b) CO_2 (left), and (c) the ratio of H_2/CO_2 (right) in the photocatalytic reaction test with Pt(0.05)/CTO(KCl, 50) sample.

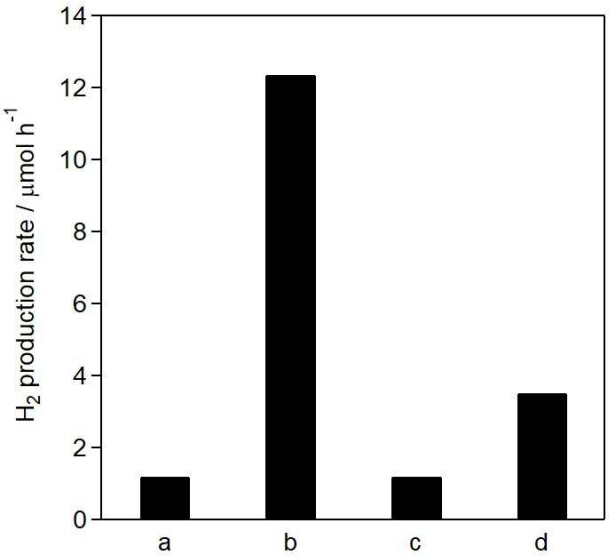

Fig. 5. Hydrogen production rate in PSRM with the Pt(0.05)/CTO(*flux*, 50) samples, (a) Pt(0.05)/CTO(NaCl, 50), (b) Pt(0.05)/CTO(KCl, 50), and (c) Pt(0.05)/CTO($CaCl_2$, 50), and (d) the Pt(0.05)/CTO(SS) sample.

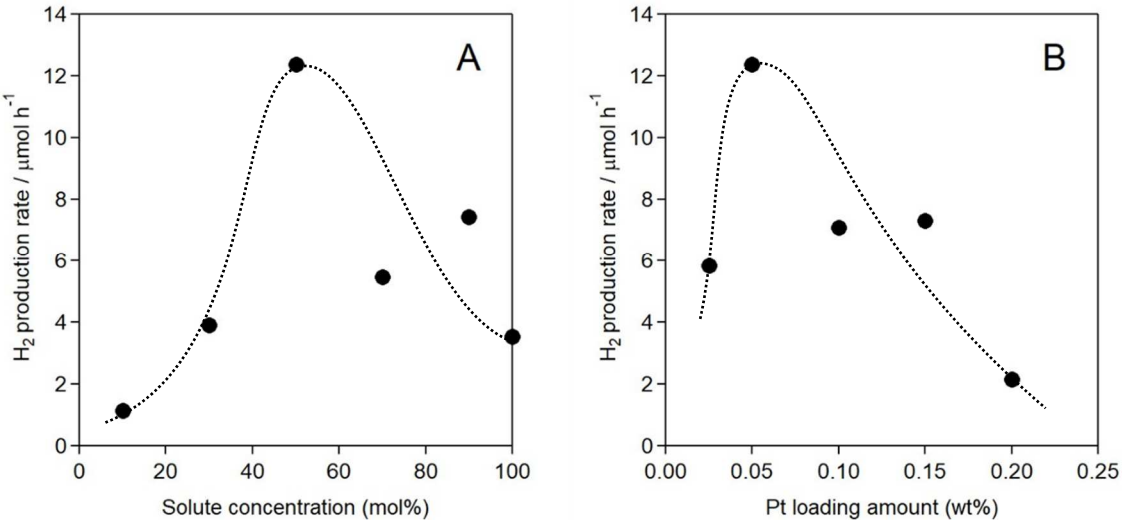

Fig. 6. Hydrogen production rate in PSRM with (A) the Pt(0.05)/CTO(KCl, *y*) samples prepared by a flux method with various solute concentration (*y* mol%) in a KCl flux, and (B) the Pt(*x*)/CTO(KCl, 50) samples of various Pt loading amount (*x* wt%).

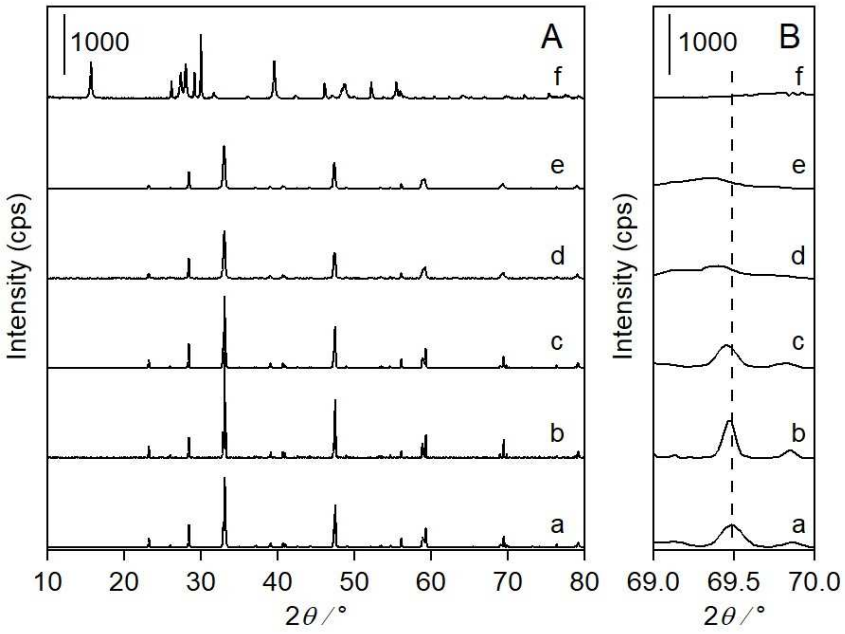

Fig. 7. XRD patterns of the CTO:La(*x*, KCl, 50) samples in the range of (A) 10°–80° and (B) 69°–70°, where La doping amount *x* was (a) 0, (b) 0.5, (c) 1, (d) 3, and (e) 5 mol %, and (f) La_2O_3 as a reference.

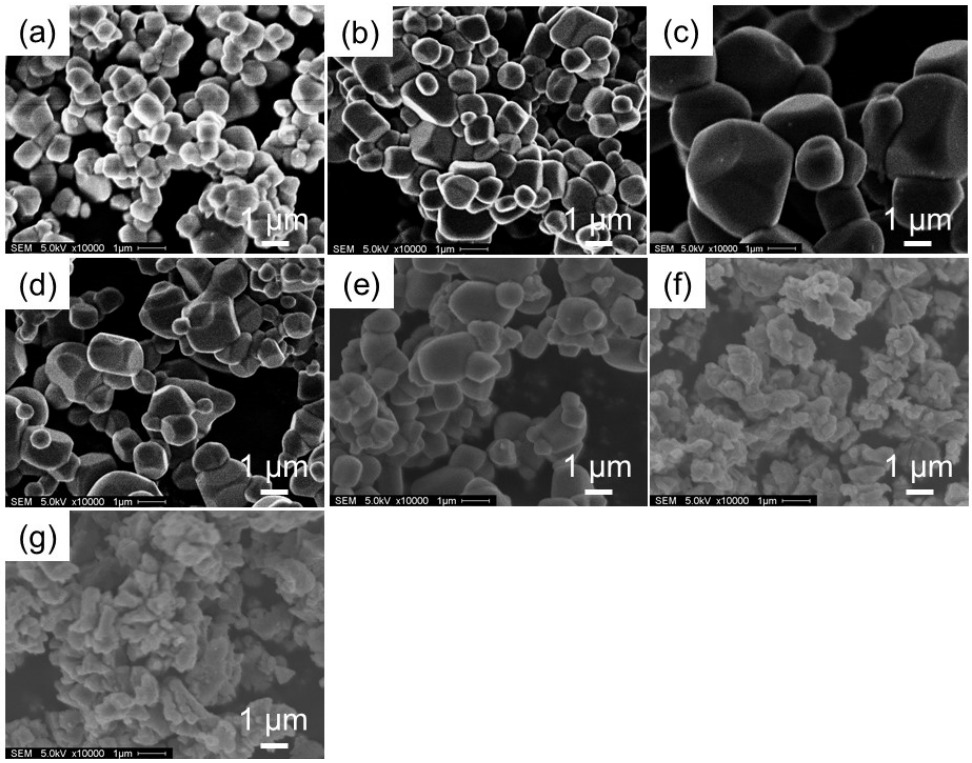

Fig. 8. SEM images of the CTO:La(*x*, KCl, 50) samples with different La doping amount *x*; (a) 0, (b) 0.1, (c) 0.5, (d) 0.7, (e) 1, (f) 3, and (g) 5 mol%.

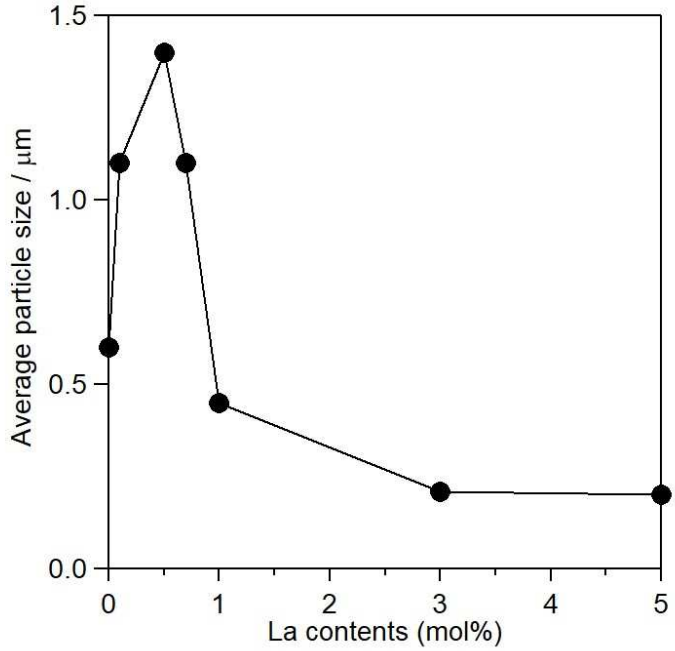

Fig. 9. The average particle size determined from SEM images of the CTO:La(*x*, KCl, 50) samples with different La doping amount (*x* mol%).

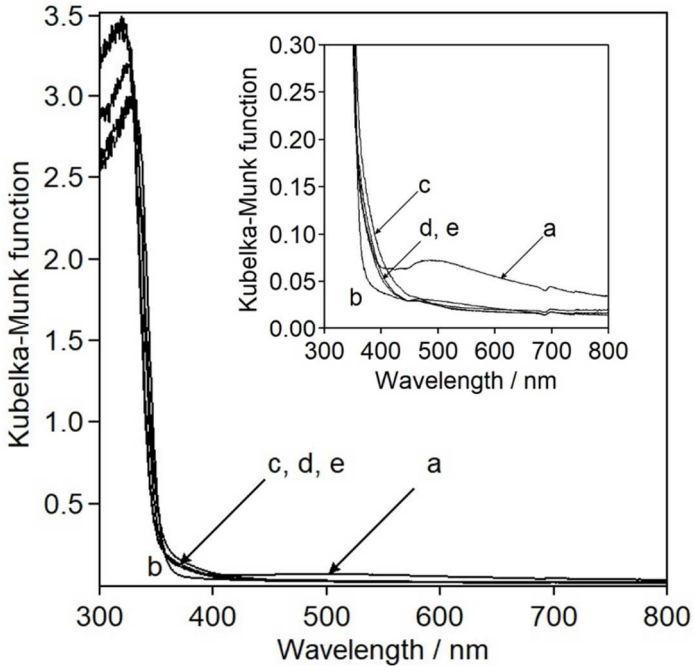

Fig. 10. DR UV-visible spectra of the CTO:La(*x*, KCl, 50) samples with different La doping amount *x*; (a) 0, (b) 0.5, (c) 1, (d) 3, and (e) 5 mol%.

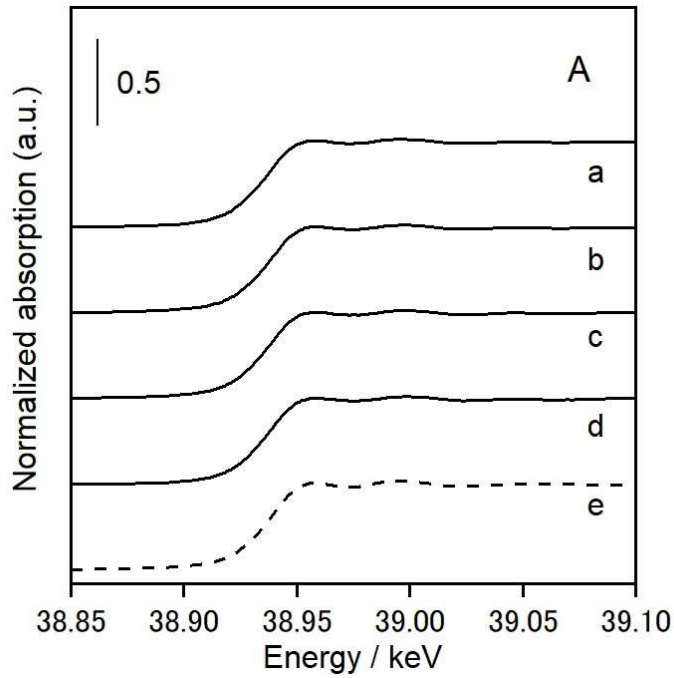
0.5
A
a
b
c
d
e
Normalized absorption (a.u.)
38.85
38.90
38.95
39.00
39.05
39.10
Energy / keV

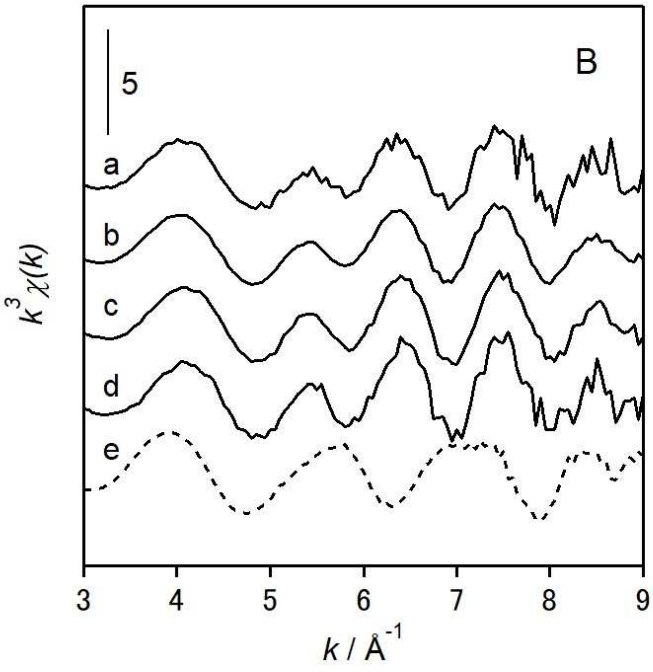
5
B
a
b
c
d
e
$k^3\chi(k)$
3
4
5
6
7
8
9
k / Å^{-1}

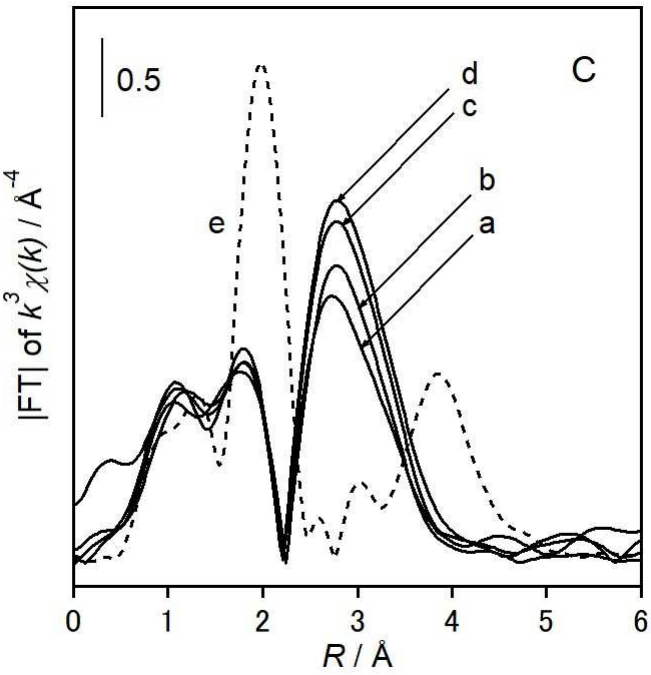

Fig. 11. (A) La K-edge XANES spectra, (B) EXAFS oscillations, and (C) Fourier transforms of the EXAFS oscillation for the CTO(*x*, KCl, 50) samples, where La doping amount *x* was (a) 0.5, (b) 1, (c) 3, and (d) 5 mol%, and (e) those for La_2O_3 as a reference.

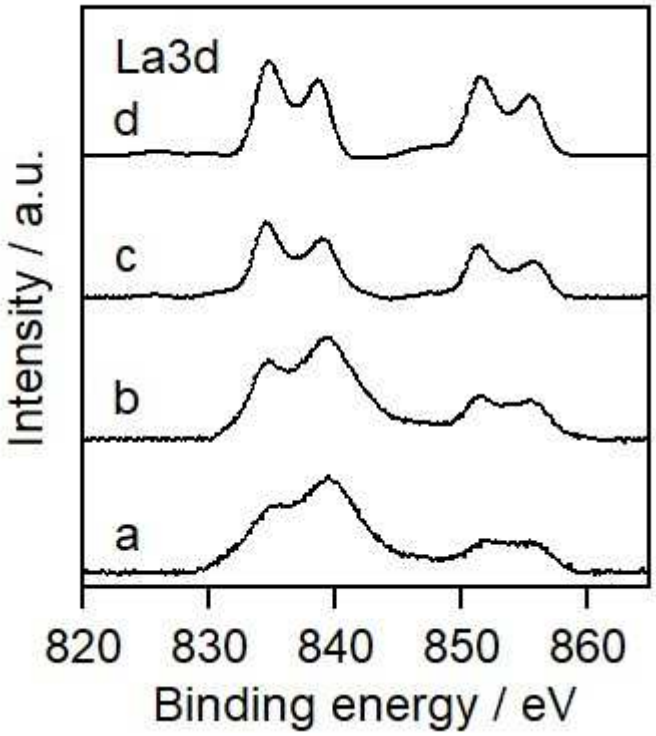

Fig. 12. La 3d bands XPS spectra of the CTO(*x*, KCl, 50) samples with La doping amount x; (a) 0.5, (b) 1, and (c) 5 mol%, and (d) that of La_2O_3 as a reference.

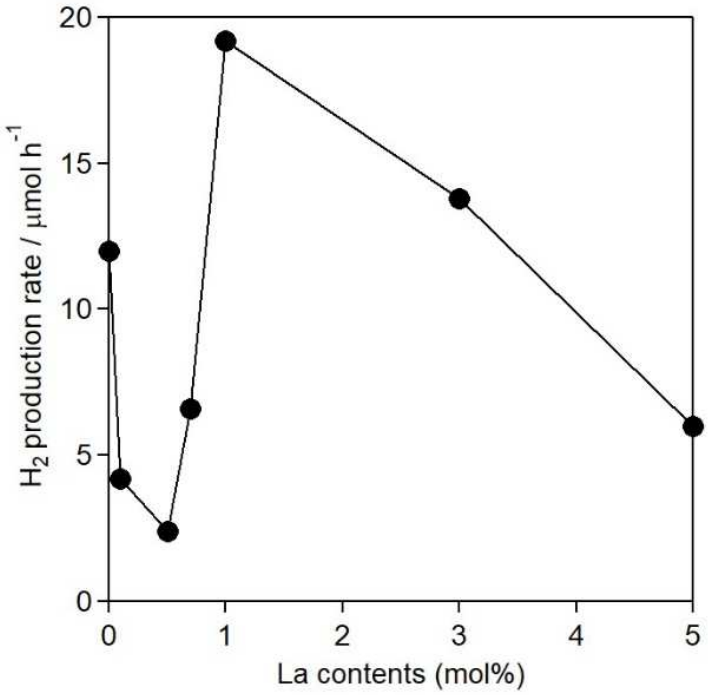

Fig. 13. Hydrogen production rate in PSRM with the Pt(0.05)/CTO:La(*x*, KCl, 50) samples prepared by a flux method with various La contents (*x* mol%).